Journal of Geophysical Research: Solid Earth

RESEARCH ARTICLE
10.1029/2018JB015654

Stability and Reactions of $CaCO_3$ Polymorphs in the Earth's Deep Mantle

Zhigang Zhang[1,2,3], Zhu Mao[4], Xi Liu[5,6], Yigang Zhang[1,2,3], and John Brodholt[7,8]

[1]Key Laboratory of Earth and Planetary Physics, Institute of Geology and Geophysics, Chinese Academy of Sciences, Beijing, China, [2]Institutions of Earth Science, Chinese Academy of Sciences, Beijing, China, [3]College of Earth and Planetary Sciences, University of Chinese Academy of Sciences, Beijing, China, [4]Laboratory of Seismology and Physics of Earth's Interior, School of Earth and Planetary Sciences, University of Science and Technology of China, Hefei, Anhui, China, [5]Key Laboratory of Orogenic Belts and Crustal Evolution, MOE, Peking University, Beijing, China, [6]School of Earth and Space Sciences, Peking University, Beijing, China, [7]Department of Earth Sciences, University College London, London, UK, [8]Centre for Earth Evolution and Dynamics (CEED), University of Oslo, Oslo, Norway

Key Points:
- The phase boundaries of $CaCO_3$ polymorphs are sensitive to temperature at high pressures
- At high temperatures, the high pressure restabilization of $CaCO_3$ over $MgCO_3$ is found to be unfavorable
- $CaCO_3$ polymorphs readily reacts with SiO_2 even in the cold subduction slabs down to the Earth's deep mantle

Supporting Information:
- Supporting Information S1
- Data Set S1
- Data Set S2

Correspondence to:
Z. Zhang,
zgzhang@mail.iggcas.ac.cn

Citation:
Zhang, Z., Mao, Z., Liu, X., Zhang, Y., & Brodholt, J. (2018). Stability and reactions of $CaCO_3$ polymorphs in the Earth's deep mantle. *Journal of Geophysical Research: Solid Earth*, *123*. https://doi.org/10.1029/2018JB015654

Received 13 FEB 2018
Accepted 22 JUL 2018
Accepted article online 1 AUG 2018

Abstract As an important component of carbonates in the mantle, $CaCO_3$ is a major carrier of carbon from the surface to the deep interiors. In recent years, new varieties of $CaCO_3$ polymorphs have been continuously predicted by first principles simulations and verified by experiments. The findings of these polymorphs open the possibility of stabilizing $CaCO_3$ component in the lowermost mantle. Here, through extensive first principles simulations, we inspect the stability and reactions of high-pressure $CaCO_3$ polymorphs at high temperatures. Systematic errors from approximations to the exchange-correlation functional in density functional theory have been essentially eliminated with a generalized rescaling method to increase the predictability of the simulations. We find temperature has important effects on the stabilities and the reactions of $CaCO_3$ polymorphs with mantle minerals. In particular, the tetrahedrally structured $CaCO_3$-polymorph (space group $P2_1/c$) is found to be sensitive to temperature with a positive Clapeyron slope of 15.81(6) MPa/K. Reacting with $MgSiO_3$, $CaCO_3$ is shown to be less stable than $MgCO_3$ over the whole mantle pressures (to ~136 GPa) above ~1500 K. And $CaCO_3$ is demonstrated to readily react with SiO_2 even in the cold subduction slabs. Thus, high temperature greatly increases the tendency of partitioning calcium into the silicates, and $CaCO_3$ is not likely to be the major host of carbon in the Earth's deep mantle.

1. Introduction

$CaCO_3$ is a common component in rocks at the Earth's surface and in the marine sediments. Through the transport of altered oceanic lithosphere and carbonaceous sediments in subduction zones, it can be cycled into the mantle and may have impacts as far down to the transition zone or lower mantle as inferred from inclusions in the sublithospheric minerals and diamonds (Brenker et al., 2007; Kaminsky, 2012; Zedgenizov et al., 2016). As a vital proxy of carbon (Keppler et al., 2003; Luth, 1999), $CaCO_3$ is important not only in connecting the surficial volatiles with those in the Earth's interiors (Luth, 1999, 2014), but also in the melting in the mantle (Hammouda & Keshav, 2015), and may be closely related with the formation of super-deep diamonds (Walter et al., 2011). The phase relations of $CaCO_3$ and its reactions with other minerals are indispensable to quantitatively understand the roles played by $CaCO_3$ in the deep mantle.

Through decades of experimental and theoretical efforts, current knowledge of phase relations in carbonate systems advance significantly (see Shatskiy et al., 2015, and references therein). For the end-member $CaCO_3$, recent studies at high pressures demonstrate that it shows more complex structures and has a greater variety of polymorphs than expected. Besides the well-known calcite (and related metastable phases calcite I–III) and aragonite (Suito et al., 2001), compressed polymorphs of $CaCO_3$ have been predicted by ab initio simulations (Oganov et al., 2006, 2008) and verified by high pressure experiments (Merlini et al., 2012; Ono et al., 2007). Pickard and Needs (2015) carried out calculations using ab initio random structure searching technique and discovered some additional monoclinic $CaCO_3$-polymorphs that are more stable at the pressures of the topmost and lower part of the lower mantle. Through state-of-the-art in situ experimental techniques, these new phases or their analogues have been observed in several most recent studies (Gavryushkin et al., 2017; Li et al., 2018; Lobanov et al., 2017). Despite the findings of these high-pressure polymorphs, there are still significant uncertainties as to the stability of $CaCO_3$-polymorphs at simultaneously high pressures and high temperatures and remarkable discrepancies still exist in the phase boundaries constrained from different approaches (Li et al., 2018).

The greater variety of $CaCO_3$-polymorphs as compared with other carbonate components increases the possibility that $CaCO_3$ may be stable at high pressures in the lower mantle (Oganov et al., 2008; Pickard & Needs, 2015). Considering the major minerals in the lower mantle and basaltic subduction slabs, three typical reactions are relevant (Oganov et al., 2008):

(R1) $$CaCO_3 + MgO = CaO + MgCO_3,$$

(R2) $$CaCO_3 + MgSiO_3 = CaSiO_3 + MgCO_3,$$

(R3) $$CaCO_3 + SiO_2 = CaSiO_3 + CO_2 \text{ or } CaCO_3 + SiO_2 = CaSiO_3 + C + O_2.$$

Previous theoretical calculations find that the reactants in reactions (R1) and (R3) are more stable relative to the products over the mantle pressures (Oganov et al., 2008; Pickard & Needs, 2015). They also show that the stability of $CaCO_3$ over $MgCO_3$ in reaction (R2) can be achieved above ~100 GPa (Pickard & Needs, 2015). Thus, $CaCO_3$ could be restabilized and become the main host of carbon in the lowermost mantle. This is opposed to extrapolations from experiments at modest pressures (Biellmann et al., 1993; Li et al., 2018). Since these previous simulations were carried out under static conditions (T = 0), it is unclear whether or not the predicted restabilization of $CaCO_3$ still hold at high temperatures.

To inspect the stability and reactions of $CaCO_3$ polymorphs in the Earth's deep mantle, especially at high temperatures, we systematically investigated the phase boundaries of the $CaCO_3$ and the reaction lines of ((R1)–(R3)) over mantle T–P conditions in this study. Extensive first principles lattice dynamics (LD) and molecular dynamics (MD) simulations have been carried out to comprehensively clarify the temperature effects. Our calculations in this study demonstrate that $CaCO_3$ readily reacts with silicates even along the temperature profiles in cold subduction slabs and therefore cannot be the major host of carbon in the deep mantle.

2. Methods

2.1. Candidate Phases and Nomenclatures

Based on previous theoretical studies (Oganov et al., 2006, 2008; Pickard & Needs, 2015) and experiments (Merlini et al., 2012; Ono et al., 2005, 2007), we consider eight high pressure polymorphs of $CaCO_3$ that are relevant to the mantle conditions in this study, namely aragonite (space group *Pmcn*), "aragonite-II" (space group $P2_1/c$), "postaragonite" (space group *Pmmn*), "$CaCO_3$-$P2_1/c$-l," "$CaCO_3$-*Pnma*-h," "$CaCO_3$-$P2_1/c$-h," "pyroxene-type" (space group $C222_1$), and "$CaCO_3$-VI" (space group $P\bar{1}$). Since most of these polymorphs have no official names yet, we use the same nomenclatures (nonofficials with quotation marks) as in the previous studies for better references. In particular, the aragonite-II phase is a distorted structure of aragonite proposed by Gavryushkin et al. (2017); the postaragonite phase corresponds to that examined in the experiments by Ono et al. (2005) and simulations by Oganov et al. (2006); the phases of $CaCO_3$-$P2_1/c$-l, $CaCO_3$-*Pnma*-h, and $CaCO_3$-$P2_1/c$-h are those predicted by Pickard and Needs (2015), among which the $CaCO_3$-$P2_1/c$-l phase is similar to the $CaCO_3$-VII phase observed by Gavryushkin et al. (2017) and Li et al. (2018) and the $CaCO_3$-$P2_1/c$-h phase is closely related with that detected by Lobanov et al. (2017); the pyroxene-type phase corresponds to the *phase I* predicted by Oganov et al. (2006) and may be relevant to that found by Ono et al. (2007); and finally the $CaCO_3$-VI phase, as found by Merlini et al. (2012), is similar to the *phase II* predicted by Oganov et al. (2006). For convenience, all these structures are provided in the supporting information Data Set S1 in the form of crystallographic information files.

2.2. Simulations

First principles simulations are carried out with VASP with the projector-augmented-wave method (Kresse & Joubert, 1999). We focus on the Local Density Approximation (LDA) in this study and eliminate the systematic errors through the well-established rescaling method proposed in our previous studies (Zhang et al., 2013; Zhang & Liu, 2015). The core radii are 2.3 au for Ca (with [Ne] core), 1.5 au for C (with [He] core), and 1.52 au for O (with [He] core).

Lattice constants and internal coordinates in the unit cells of the $CaCO_3$ polymorphs at static conditions are fully relaxed with an energy cutoff of 1,000 eV for the plane wave basis set and a

convergence criterion of 10^{-8} eV for the electronic self-consistent loop. We use a Brillouin zone sampling grid of spacing 0.3 $Å^{-1}$, which is well converged as revealed by our benchmarks with finer spacing of 0.2 $Å^{-1}$.

LD simulations are carried out through finite displacement method with the aid of the package Phonopy (Togo & Tanaka, 2015). The interatomic force constants are calculated by setting a displacement amplitude of 0.01 Å for each atom. The supercell is defined with the length of each lattice vector larger than 8 Å and therefore contains 80–160 atoms (details of the constructed supercells and number of atoms for the eight polymorphs are listed in Table S1). To evaluate the vibrational density of state, a $32 \times 32 \times 32$ mesh is used for the *q*-point sampling in the first Brillouin zone. In the framework of quasi-harmonic approximation theory, we can conveniently obtain various thermodynamic properties at finite temperatures through options provided by Phonopy. The generated parameters for the Birch-Murnaghan equation of state (EOS) from 300 to 900 K can be found in Data Set S2.

We have also carried out extensive MD simulations from 1000 to 3500 K to account for possible anharmonicity that may be important at high temperatures (Zhang et al., 2013). The equivalent supercells used in the above-mentioned phonon calculations are constructed for the MD simulations. At each time step (1 fs interval), the electronic structure is calculated at the Brillouin zone center with an energy cutoff of 500 eV and iteration convergence criterion of 10^{-6} eV. MD trajectories are propagated in the *NVT* ensemble with the Nosé thermostat for 5–10 ps, with the first 3 ps discarded for pre-equilibrium. Larger supercells and longer durations generate unchanged properties within the statistical uncertainties. We carefully inspect the simulated structures in the MD trajectories to ensure that the phase is maintained without transitions during the calculations of the thermodynamic properties. These MD simulation results are regressed with the following Mie-Gruneisen EOS:

$$P(V,T) = P_C(V,T_s) + \frac{\gamma}{V} C_V (T - T_s), \tag{1}$$

where P_C is the reference isotherm at T_s = 900 K (also serve as the switching temperature as mentioned in section 3.1) that can be accurately reproduced with the Birch-Murnaghan EOS, γ is the Gruneisen parameter and we simplify it to be linear with V by $\gamma = \gamma_a + \gamma_b^*(V - V_{s0})/V_x$ (V_{s0} is the volume at zero pressure and T_s; V_x is an arbitrary auxiliary parameter, which is chose here to be 40.1873 cm^3/mol as consistent with our previous study; Zhang & Liu, 2015), and C_V is the isochoric heat capacity. Keeping the parameters at T_s the same as those by LD simulations, we regress the pressures and internal energy differences with respect to those at T_s and get the parameters as listed in Table S2.

2.3. Correction to the Simulation Results

It is well known that LDA typically over-binds structures and therefore usually underestimates the volumes in a wide variety of systems. As discussed in our previous studies (Zhang et al., 2013; Zhang & Liu, 2015), a generalized rescaling method can be used to effectively eliminate the systematic errors in the simulated volumes. The rescaling provides results that are essentially independent of the choice of exchange-correlation functional, and is needed for obtaining experimentally accurate results. If we choose the aragonite phase as a reference phase and 300 K as a reference temperature (T_0 = 300 K), and by assuming the systematic errors depend only on the volume and are the same for all phases, we get the following relationships for the Helmholtz free energy and pressure:

$$F(V,T) = F^{LDA}(V,T) - F^{LDA}_{arag}(V,T_0) + F_{arag}(V,T_0), \tag{2}$$

$$P(V,T) = P^{LDA}(V,T) - P^{LDA}_{arag}(V,T_0) + P_{arag}(V,T_0). \tag{3}$$

The left-hand side is the corrected value for the phase of interest at V and T, and the first term on the right-hand side is the calculated value for the same phase at the same V and T. The next two terms make up the correction to the LDA results based on the calculated (LDA) and expected properties of aragonite, respectively. The expected results of F_{arag} and P_{arag} at T_0 can be further evaluated by rescaling the corresponding simulated results:

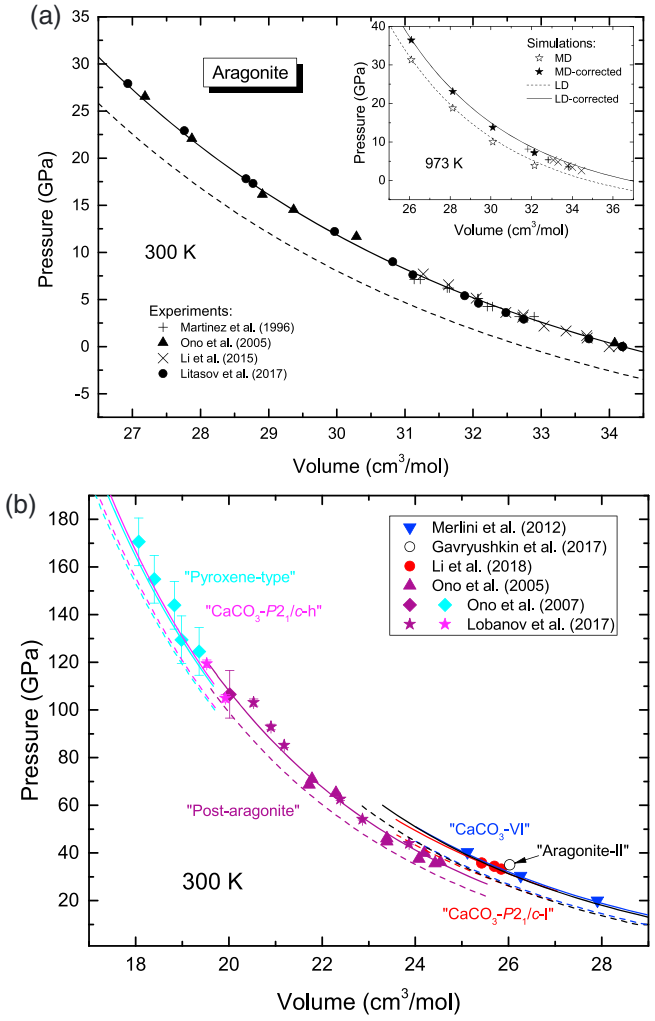

Figure 1. Comparisons between the simulations in this study and the experiments in the literature (Gavryushkin et al., 2017; Li et al., 2015; Li et al., 2018; Litasov et al., 2017; Lobanov et al., 2017; Martinez et al, 1996; Merlini et al., 2012; Ono et al., 2005; Ono et al., 2007): (a) aragonite at 300 and 973 K (inset); (b) other polymorphs at 300 K. The dashed curves and open stars (at 973 K) are the raw results by LD simulations and MD simulations, respectively. We apply the rescaling corrections to these raw results and obtain the solid curves and filled stars. The parameters for the rescaling (equations (2)–(5)) are V_0^{exp} = 34.20 cm^3/mol and K_0^{exp} = 67.1 GPa (from Ono et al., 2005); V_0^{LDA} = 32.75 cm^3/mol and K_0^{LDA} = 75.0 GPa. In (b), we plot the data (experiments with points and simulations with lines) for polymorphs in different colors: "$CaCO_3$-VI" in blue, "aragonite-II" in black, "$CaCO_3$-$P2_1/c$-l" in red, "postaragonite" in purple and "pyroxene-type" in cyan. Data for the "$CaCO_3$-$P2_1/c$-h" phase, which is closely similar with the pyroxene-type phase, are also shown in magenta. Note that the pressures of the experiments by Ono et al. (2005, 2007) are recalculated with a more accurate pressure-scale proposed by Fei et al. (2007). LD = lattice dynamics; MD = molecular dynamics.

$$F_{arag}(V,T_0) = F_{arag}(V_0^{exp},T_0) + \frac{V_0^{exp}K_0^{exp}}{V_0^{LDA}K_0^{LDA}}\left[F_{arag}^{LDA}\left(V\frac{V_0^{LDA}}{V_0^{exp}},T_0\right) - F_{arag}^{LDA}(V_0^{LDA},T_0)\right], \quad (4)$$

$$P_{arag}(V,T_0) = \frac{K_0^{exp}}{K_0^{LDA}}P_{arag}^{LDA}\left(V\frac{V_0^{LDA}}{V_0^{exp}},T_0\right), \quad (5)$$

where subscript 0 refers to properties of aragonite at zero pressure and 300 K and K is the isothermal bulk modulus. Note that in equation (4) there is still an unknown parameter of $F_{arag}(V_0^{exp},T_0)$ for deriving the absolute free energy. For the calculations of a one-component phase diagram, as presented in the next section, only the relative magnitude of the free energy is needed so that we can arbitrarily choose it to be $F_{arag}^{LDA}(V_0^{LDA},T_0)$. The choices of other parameters in these formulas are described in the caption of Figure 1.

3. Results and Discussion

3.1. Phase Diagram of $CaCO_3$

Many experimental measurements have been accumulated for aragonite, which facilitates a comparison with our simulations. We show in Figure 1a that the simulations with the LDA underestimate the pressures by about 3–5 GPa over the T–P regime involved in the presently available experiments for aragonite. These volume-dependent systematic errors can be essentially eliminated through our above-mentioned rescaling corrections, even for higher-temperature conditions (as revealed in the inset plot of Figure 1a) and for other higher-pressure polymorphs (as shown in Figure 1b). The success for the achieved accuracies in high pressure polymorphs is remarkable and important since most other polymorphs considered in this study have few or even no experimental data, especially at very high temperatures and pressures.

With a closer inspection over the high temperature data of the corrected results in the inset plot of Figure 1a, it can be found that the LD simulations predict slightly higher pressures at large volumes while those simulated by MD are in very good agreement with the experiments; this implies an increasingly prominent influence of anharmonicity. To combine the merits of both approaches, we choose a switching temperature (T_s) of 900 K, below which we adopt the LD simulation results to accurately account for the quantum effects and above which we use the thermal properties (respect to T_s) by MD simulations to implicitly account for the possible anharmonicity. While it is possible to adopt more rigorous calculations for the anharmonicity at high temperatures (i.e., Monserrat et al., 2013; Zhang et al., 2014), the simple way of combining the LD and MD simulations would be adequate for the purpose of this study.

The relative stabilities of the polymorphs considered in this study were evaluated from their Gibbs free energies. Applying the corrections to the systematic errors, we obtain the free energy curves relative to that of aragonite, as shown in Figure 2. At 300 K, aragonite transforms to the $CaCO_3$-$P2_1/c$-l phase at 23.6 GPa and then to the postaragonite phase at 45.2 GPa. When pressure is further increased to 56.4 GPa, the $CaCO_3$-$P2_1/c$-h phase becomes stable and persists to higher pressures. Increasing temperature to 2000 K slightly lowers the pressure of the first two phase transitions to about 19.4 and 42.1 GPa but significantly broadens the phase regime of the postaragonite phase to 87.4 GPa. The other four phases are unstable over the pressure and

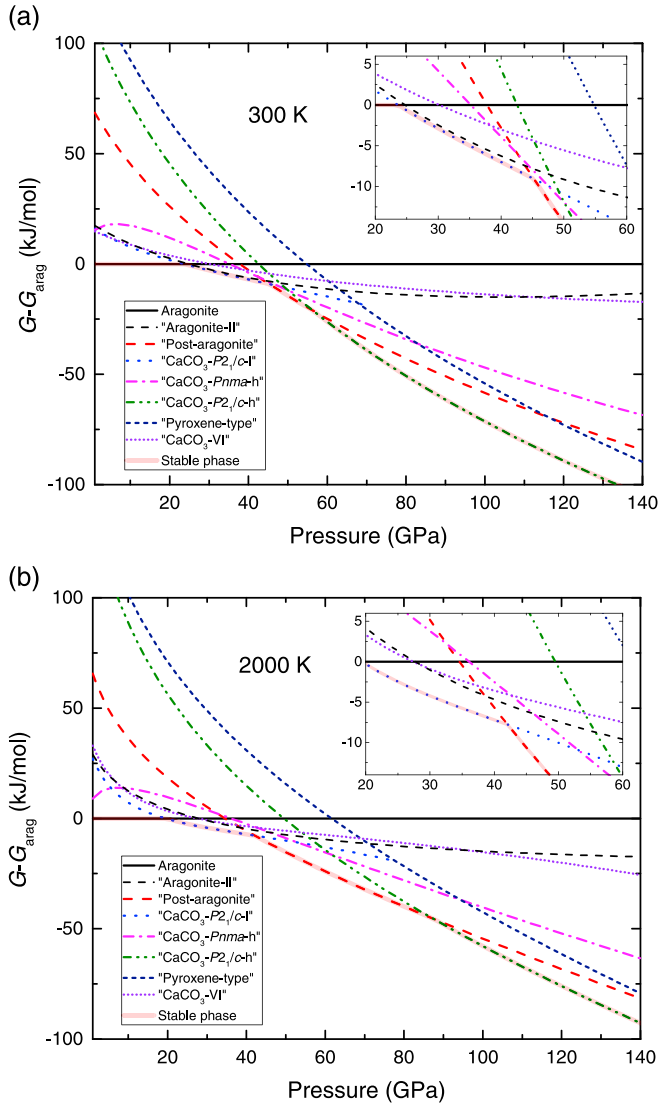

Figure 2. Gibbs free energies of $CaCO_3$ polymorphs relative to that of aragonite at (a) 300 and (b) 2000 K. The thermodynamic stable phase with the lowest Gibbs free energy is marked with shaded red line. Insets are the focused plots within the pressure regime of 20–60 GPa to show the small free energy differences more clearly.

temperature range considered in this study. Among them, the aragonite-II phase is only marginally unstable relative to the stable phase with a minimum free energy difference of only about 0.4 kJ/mol (i.e., 0.8 meV per atom) in the vicinity of 30–40 GPa at 300 K. It should be noted that Gavryushkin et al. (2017) find the stability of aragonite-II phase in similar pressure range at 0 K. The apparent discrepancy can be ascribed to the different simulation details and also such small energetic differences. At 2000 K, the energy difference increases to larger than 2.5 kJ/mol (i.e., 5 meV per atom), which means the aragonite-II phase becomes increasingly unstable at high temperatures. The $CaCO_3$-*Pnma*-h phase similarly approaches quite near the stable phase right around the phase transition from the $CaCO_3$-$P2_1/c$-I phase to the postaragonite phase with minimum free energy differences of about 1.0 and 4.0 kJ/mol at 300 and 2000 K, respectively. The $CaCO_3$-VI phase also approaches the stable phase at around 24 GPa, where the aragonite begins to be unstable, with minimum free energy differences of about 2.4 and 3.3 kJ/mol at these two temperatures. The pyroxene-type phase, which resembles the $CaCO_3$-$P2_1/c$-h phase with fourfold coordinated carbon atoms, seems to be quite unstable with a free energy significantly higher than that of the stable phases by over 13.5 kJ/mol.

By connecting the intersections of the free energy curves, we obtain the phase diagram of $CaCO_3$ in Figure 3. The transition pressures between the phase $CaCO_3$-$P2_1/c$-I and its neighborhoods (aragonite at the lower pressure side and postaragonite at the higher pressure side) are relatively insensitive to temperature. The Clapeyron slopes of the boundaries are slightly negative and are around −1.97(4) MPa/K, which is quite close to the most recent experimental measurements (Li et al., 2018). The upper phase boundary of the postaragonite phase, on the other hand, is very sensitive to temperature, with an average Clapeyron slope of 15.81(6) MPa/K. Compared with the transition slopes, the absolute positions of the phase boundaries have more uncertainty since the free energy differences between the adjacent phases are small around the transition points. We have evaluated the uncertainties of the phase boundaries by considering a typical error of 2 kJ/mol in the calculated free energy contrast of the coexisting phases. As shown in Figure 3, within the uncertainties, the predicted phase regions agree quite well with those experimentally determined for the postaragonite phase (Ono et al., 2005). For the $CaCO_3$-$P2_1/c$-I phase, its upper boundary is predicted in good agreement with recent experiments (Gavryushkin et al., 2017; Li et al., 2018), while its lower boundary is slightly lower than that determined by Li et al. (2018) and remarkably lower than that observed by Gavryushkin et al. (2017). The recent experimental observation of the $CaCO_3$-$P2_1/c$-h phase (Lobanov et al., 2017) lies right at the predicted phase regime in this study, while the onset of the transition pressure (~103 GPa at ~2000 K) is higher than the predicted boundary here (~87.4 ± 6.6 GPa).

3.2. Kinetic Effects for the Stability of $CaCO_3$

Compared with silicates, carbonates show much complexity with more varieties of reversible metastable transitions, which introduces challenges for experimental measurements and theoretical predictions. Through our calculations in this study, we have found that the free energy differences among adjacent polymorphs are very small. As mentioned above, the $CaCO_3$-VI phase excluded from the phase diagram in Figure 3 is actually only slightly unstable relative to the stable phases (Figure 2). Therefore, its presence in high pressure experiment from ~15 to ~40 GPa (Merlini et al., 2012) may be explained either by possible uncertainties in our calculations or by kinetic barriers of equilibrium phase transitions often encountered

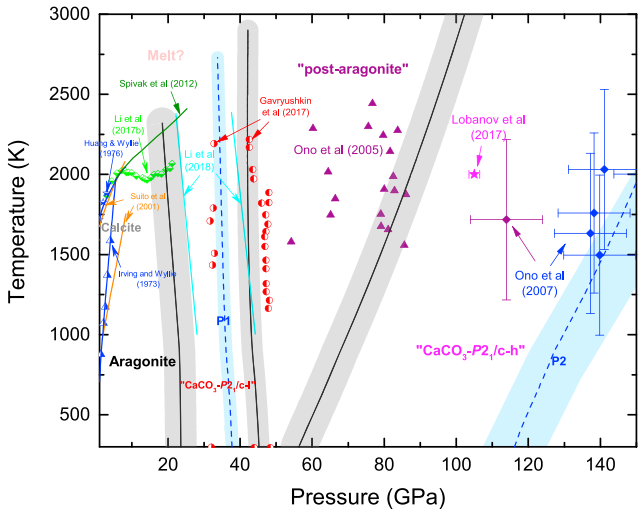

Figure 3. Phase diagram of $CaCO_3$ based on previous experimental measurements and current first principles simulations. The three black solid curves are the predicted phase boundaries of the stable polymorphs as indicated with bold colored texts. The blue dashed curves are the predicted pseudo phase boundary between the aragonite and *postaragonite* (marked as P1) and that between the postaragonite and "pyroxene-type" phases (marked as P2), as discussed in section 3.2. The shadows around these curves show the effects of uncertainties in the free energy (illustrated with a typical 2 kJ/mol here) on the predicted phase boundaries. For the experimental data, the half-filled symbols are on the phase boundaries while the filled symbols are in the one-phase field (in purple for postaragonite, in magenta for "$CaCO_3$-$P2_1/c$-h" and in blue for pyroxene-type, in red for "$CaCO_3$-$P2_1/c$-l"). The olive curve is the melting curve determined by Spivak et al. (2012), while the half-filled green diamonds are the melting curve measured by Li et al. (2017). The cyan straight lines are the phase boundaries for the $CaCO_3$-$P2_1/c$-l as estimated by Li et al. (2018). The phase boundaries for calcite are shown with three sets of experiments (Huang & Wyllie, 1976; Irving & Wyllie, 1973; Suito et al., 2001).

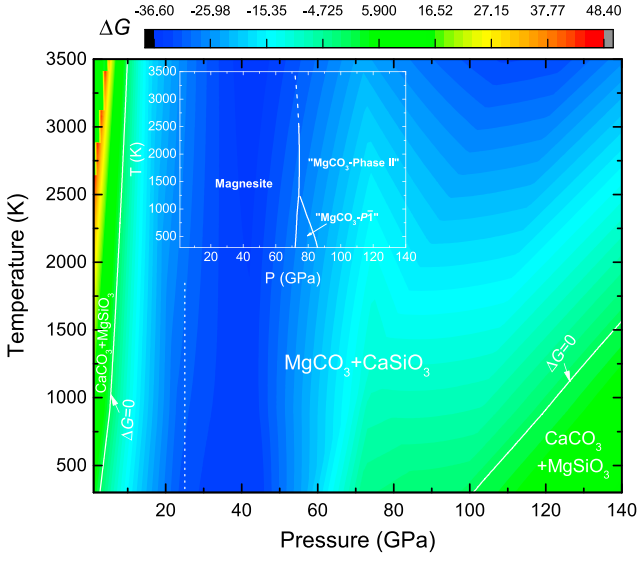

Figure 4. Relative stability of $CaCO_3$ and $MgCO_3$ from the Gibbs free energy change (ΔG) of reaction (R2). The vertical dotted line corresponds to ~25 GPa above which bridgmanite and $CaCO_3$-perovskite become stable. Simulated phase relations of $MgCO_3$ polymorphs up to 140 GPa and 3500 K are shown in the inset plot.

in the experiments (Ono et al., 2005, 2007). The observations of the aragonite-II phase in the recent experiment by Gavryushkin et al. (2017) can be explained in the same manner.

Another noticeable deviation of our calculated phase diagram from the experiments is that the predicted stable phase at highest pressures (to over 140 GPa) is not in accordance with the experimentally observed one by Ono et al. (2007). As pointed out by Pickard and Needs (2015), the limited resolution of the experimental spectrum at these extreme pressures may not allow a good discrimination between the pyroxene-type phase claimed by Ono et al. (2007) and the energetically much more stable $CaCO_3$-$P2_1/c$-h phase. Alternatively, it is possible that the discrepancy may be ascribed to the energy barriers along the possible phase transition routes taken by the experiments. Although quantitative evaluations of the kinetic reaction barriers are out of the scope of this study, the compression of $CaCO_3$ seems to follow two different phase transition routes with high barriers in between: one is the *orthorhombic phase transition route* from aragonite to postaragonite and finally to the pyroxene-type phase, while the other is the *monoclinic phase transition route* from the $CaCO_3$-$P2_1/c$-l phase to the $CaCO_3$-$P2_1/c$-h phase. The energy barriers for the phase transitions along either of these routes are likely to be small as compared to those for the phase transitions between the two routes. Indeed, the $CaCO_3$-$P2_1/c$-l phase is found to spontaneously collapse to the $CaCO_3$-$P2_1/c$-h phase at around 70–80 GPa without any energy barrier. And the recent study of Lobanov et al. (2017) proved that the barrier height between postaragonite and $CaCO_3$-$P2_1/c$-h is large. In this sense, it seems to be plausible that two additional metastable phase transition boundaries may be more relevant to the experiments interfered by the kinetic barrier problem in this pressure range. In Figure 3, the blue dashed line marked with *P1* is for the transition from the aragonite to postaragonite, and that marked with *P2* is for the transition from the postaragonite to pyroxene-type phase. The Claypayon slopes of these two phase transitions are similar to those of the phase transitions $CaCO_3$-$P2_1/c$-l-postaragonite and postaragonite-$CaCO_3$-$P2_1/c$-h, respectively. Within the uncertainties, the experimental findings by Ono et al. (2007) can be reasonably explained in this way.

3.3. Reactions (R1) and (R2)

In these two reactions, five polymorphs of $MgCO_3$ have been included in our extensive MD and LD simulations, namely, conventional magnesite (space group $R\bar{3}c$), "$MgCO_3$-phase II" (space group $C2/m$) and $MgCO_3$-phase III (space group $P2_1$) as predicted by Oganov et al. (2008), "$MgCO_3-P\bar{1}$" and "$MgCO_3$-$P2_12_12_1$" as predicted by Pickard and Needs (2015). These structures are also included in Data Set S1. Using the same approach as for $CaCO_3$ described above, we obtain a phase diagram for $MgCO_3$ composition as shown in Figure 4. The $MgCO_3$-phase III and $MgCO_3$-$P2_12_12_1$ are found to be closely equivalent in energy and are stable above ~144 GPa. Therefore, in the inset plot of Figure 4, only three polymorphs are involved and the $MgCO_3-P\bar{1}$ phase finds its stability in a limited regime, which explains the recent experiments that magnesite transforms directly to $MgCO_3$-phase II at high temperatures (Maeda et al., 2017).

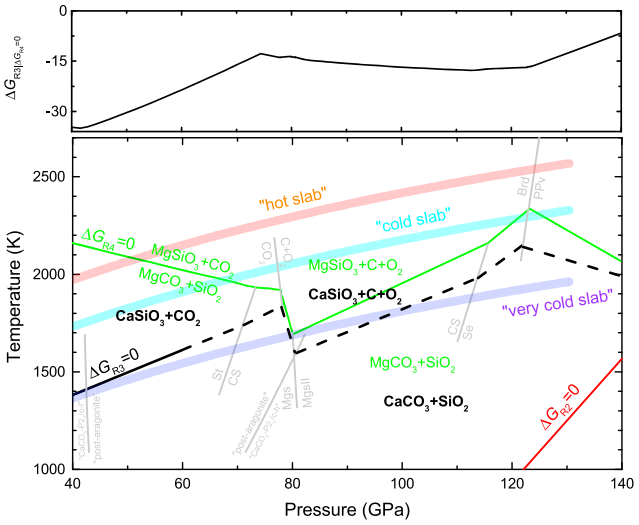

Figure 5. Schematic reaction line of ((R3)) based on the recent experimental constraints and simulated data in this study. The phase diagram of the $MgCO_3$-SiO_2 system, with measured reaction line of ((R4)) (in green) and phase boundaries of relevant phases (St: Stishovite; CS: $CaCl_2$-type SiO_2; se: Seifertite; mgs: Magnesite; MgsII: Magnesite-phase II; Brd: Bridgmanite; PPv: $MgSiO_3$-post-perovskite), follows that proposed by Maeda et al. (2017). Phase boundaries of $CaCO_3$ polymorphs predicted in this study are included with light-gray solid lines. The reaction line of ((R3)) below 60 GPa (in bold solid line) is the measured curve in our recent study (Li et al., 2018) and that above 60 GPa (in bold dashed line) is extended by considering the phase boundaries and the free energy change of reaction (R3) (ΔG_{R3}) along the reaction line of ((R4)) ($\Delta G_{R4} = 0$), as plotted on the top of the figure. The reaction line of ((R2)) ($\Delta G_{R2} = 0$) is shown in red. Geotherms of subducted slabs are shown after Maeda et al. (2017).

For the silicates and oxides in these two reactions, we calculated their free energies in the framework of quasi-harmonic approximation theory by considering the following polymorphs: $MgSiO_3$ in bridgmanite and "postperovskite" structures (Oganov & Ono, 2004; Zhang et al., 2013); $CaSiO_3$ in tetragonal perovskite *I*4/*mcm* structure (Stixrude et al., 2007); MgO in rocksalt structure; CaO in B1 (NaCl) and B2 (CsCl) structures. The core radii are 2.3 au for Ca (with [Ne] core), 2.0 au for Mg (valence configuration with p semicore valence state, $2p^6 3s^2$), 1.5 au for C (with [He] core), 1.6 au for Si (with [Ne] core), and 1.52 au for O (with [He] core). The supercells and number of atoms for these phases are listed in Table S1. The other simulation settings for $MgCO_3$, $MgSiO_3$, $CaSiO_3$, MgO, and CaO are essentially identical with those for $CaCO_3$, with LDA and projector-augmented-wave implementation of VASP and also with the aid of Phonopy.

All the simulated properties of reactants and products in these reactions are corrected using the rescaling method, with the reference free energies at standard condition ($F\left(V_0^{\exp}, T_0\right)$ in equation (4)) selected from the self-consistent thermodynamic data base compiled by Holland et al. (2013). The rescaling parameters for all the relevant compositions can be found in Table S3 ($MgCO_3$ from Fiquet and Reynard (1999), CaO from Oda et al. (1992) and the other components from Stixrude and Lithgow-Bertelloni (2011), as noted in Table S3). From the derived ΔG (free energy change) of the reaction (R1), we find the $CaCO_3$ + MgO are much more stable than CaO + $MgCO_3$ over the temperature and pressure ranges interested in this study, which means the athermal stability of the reactants as predicted by Oganov et al. (2008) and Pickard and Needs (2015) still hold at high temperatures. The ΔG of reaction (R2), on the other hand, shows more complex variations as revealed in Figure 4.

It is clear from Figure 4 that the products of the reaction (R2) are significantly more stable than the reactants from ~20 to ~50 GPa, which is in agreement with previous experimental observations over similar pressure range (Biellmann et al., 1993). At lower pressures, the trend shown in Figure 4 agrees with the experimental findings of more calcic carbonates with decreasing pressure (Luth, 1999), although this may only be regarded as illustrative since the bridgmanite and $CaSiO_3$-perovskite we considered in our calculations are only stable above ~25 GPa in the mantle (vertical dotted line). At higher pressures, the higher density of the $CaCO_3$-polymorph relative to the $MgCO_3$-polymorph greatly diminishes the free energy change of reaction (R2), especially at pressures above ~70 GPa at low temperatures. The $CaCO_3$ would be finally stabilized relative to the $MgCO_3$ at ~100 GPa at 300 K, which agrees with the calculations by Pickard and Needs (2015). On the other hand, the pressure-induced restabilization of $CaCO_3$ is found to be hindered by the entropic effects of temperature and the field of $MgCO_3$ + $CaSiO_3$ opens toward higher pressures with increasing temperature. If we further take into account the phase transformation and noticeable anharmonicity of $CaSiO_3$-perovskite (as compared with $MgSiO_3$ polymorphs; Stixrude et al., 2007), the stability region of $MgCO_3$ in reaction (R2) would be even more expanded.

3.4. Reaction (R3)

As shown in Figure 5 with the bold solid line, the reaction line of (R3) has already been tightly constrained up to over 50 GPa in our recent measurements with synchrotron X-ray diffraction in laser-heated diamond anvil cells (Li et al., 2018). To extend this line to even higher pressures without the need of modeling CO_2 and O_2, which are still inadequate and challenging (Litasov et al., 2011, 2017), we find the following reaction examined by Maeda et al. (2017)

(R4) $$MgCO_3 + SiO_2 = MgSiO_3 + CO_2 \text{ or } MgCO_3 + SiO_2 = MgSiO_3 + C + O_2$$

can be closely related to reaction (R3) by

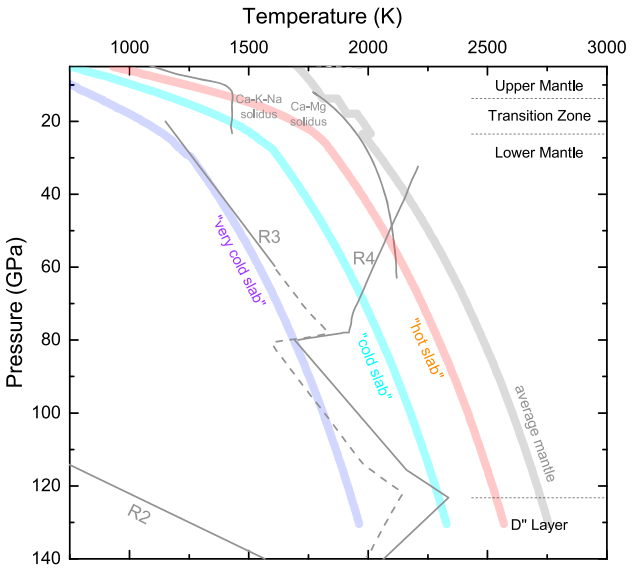

Figure 6. An integrated diagram for the reactions and meltings of $CaCO_3$ and $MgCO_3$ in the Earth's deep mantle. Besides the reaction lines of (R2)–(R4), two solidi of carbonate systems ($CaCO_3$-$MgCO_3$ marked as Ca-Mg, Thomson et al., 2014, and $(K,Na)_2Ca_4(CO_3)_5$ marked as Ca-K-Na, Litasov et al., 2013,) are included here for discussions.

$$\Delta G_{R3} = \Delta G_{R2} + \Delta G_{R4}. \quad (6)$$

Since $\Delta G_{R2} < 0$ over the mantle conditions as mentioned above, it can be inferred that the reaction line of (R3) should lie below (i.e., at lower temperature than) that of (R4), which is in accord with our measurements (Li et al., 2018). If we calculate the ΔG of reaction (R3) along the reaction line of (R4) (denoted as $\Delta G_{R3|\Delta G_{R4}=0}$), which equals ΔG_{R2} according to equation (6) since $\Delta G_{R4} = 0$, we find it approximately varies in three stages: first increases quickly from ~40 to ~75 GPa, then slightly decreases to ~120 GPa, and then further increases and finally approaches zero, as shown at the top of Figure 6. Assuming ΔG would be in proportion to the temperature (since the entropic difference (ΔS) of the reactions are relatively insensitive to the pressure), the opposite trends between the slopes of the two reactions (R3) and (R4) at relatively lower pressures can be plausibly explained by the initial increase of $\Delta G_{R3|\Delta G_{R4}=0}$. Then the slight decrease of $\Delta G_{R3|\Delta G_{R4}=0}$ in the second stage may result in a slightly departing but almost parallel extension of both reaction lines. The further increase in the third stage would gradually lead to an intersection point where the three reactions meet. With these constraints and considering the possible phase transformations of each component, using the geometric method of Schreinemakers (Zen, 1966), we finally obtain the reaction line of (R3) as shown in Figure 5.

It should be noted that this indirect way of extending the reaction line of (R3) may involve noticeable uncertainty, mostly from that of the reaction line of (R4). Although Maeda et al. (2017) constrains the decarbonation reaction boundaries of $MgCO_3$ much more precisely with increased number of high *T–P* measurements as compared with its previous studies (e.g., Seto et al., 2008), the temperature and pressure uncertainties for each data point are still remarkable (up to 10 GPa and 370 K, see Figure 2 and Table S1 of Maeda et al., 2017). The steep gradient of decomposition boundary of CO_2 as shown in Figure 5, in particular, should be highly uncertain and is apparently inconsistent with the previous estimations (Litasov et al., 2011). On the other hand, since we have precise estimations of the reaction boundary up to ~60 GPa, and the decomposition slope of CO_2 seems to reach a consensus to be negative (see Figure 4 in Litasov et al., 2011), the higher pressure extension of the reaction line would not significantly deviate from that depicted in Figure 5, as demonstrated in Figure S1.

3.5. Implications for the Fate of $CaCO_3$ in the Deep Mantle

From the new constraints obtained in this study and taking into account the solidi of carbonate systems (Litasov et al., 2013; Thomson et al., 2014), as shown in the integrated diagram in Figure 6, we may obtain a clearer picture on the fate of $CaCO_3$ in the deep mantle.

First, a large proportion of $CaCO_3$ component would be transported and melted along with the other carbonate components in many slabs up to the top region of the lower mantle (~20 GPa, rarely to ~50 GPa, as enclosed by the solidi of the $CaCO_3$-$MgCO_3$ system and alkaline carbonate). As noticed by Litasov (2011) and Kakizawa et al. (2015), possible melting reactions of $CaCO_3$ and $MgCO_3$ with silicates in the pressure range of 6–30 GPa may also take effects. Rapidly percolating through the surrounding mantle and moving upward due to their buoyancy (Hammouda & Laporte, 2000), the generated calcic carbonatite melts are closely related with the formation of diamond (Hammouda & Keshav, 2015; Rohrbach & Schmidt, 2011; Thomson et al., 2016).

Second, a few $CaCO_3$ component survived from melting in the cold slabs would readily react with $MgSiO_3$ and SiO_2. Due to the temperature effects, calcium prefers to be partitioned into the silicates as $CaSiO_3$ (e.g., through reactions (R2) and (R3)). Different from redox melting and freezing (Rohrbach & Schmidt, 2011), these reactions of $CaCO_3$ provide alternative route to produce deep diamonds or deep volatiles of CO_2 or O_2.

Third, when $CaCO_3$ is transported in the *very cold* slabs with very low temperatures, the free energy changes of reactions (R2) and (R3) are small. Taking into account the sluggish kinetics in solid phases, the occurrences

of $CaCO_3$-bearing solid solutions with other carbonate components in these slabs cannot be fully excluded but should be highly specific.

4. Conclusions

In this study, we have calculated the thermodynamic properties of $CaCO_3$ with extensive first principles simulations over wide range of temperatures and pressures. The rescaling method we proposed to eliminate the systematic errors in the simulated results shows its success in predicting various properties that are in good agreement with experiments and facilitates the precise comparisons among different data sets. The combination of LD and MD simulations provides a simple way to calculate the free energy with anharmonicity and increases the accuracy of calculated properties at high temperatures.

Based on these methods, we derive the phase diagram of $CaCO_3$ that is in accord with most recent experiments and suggest that kinetic effects may influence the experimental determined phase transitions. The phase boundaries of sp^3 bonding tetrahedrally structured high pressure polymorphs (the $CaCO_3$-$P2_1/c$-h phase and the pyroxene-type phase) are found to be sensitive to temperature. These results clarify the strong temperature effects that have not been systematically explored before and provide new constraints on the stability of $CaCO_3$ under deep mantle conditions.

Finally, we find that high temperature greatly increases the tendency of partitioning calcium of $CaCO_3$ into the silicates and produce $CaSiO_3$. From both the reactions with $MgSiO_3$ and SiO_2, $CaCO_3$ turns out to be less stable relative to the other forms of carbon ($MgCO_3$, CO_2, or C) over mantle conditions. Different from the findings of previous theoretical predictions, $CaCO_3$ cannot be restabilized even in the cold slabs and thus is not the major host of carbon in the Earth's deep mantle.

Acknowledgments
We acknowledge support from the Strategic Priority Research Program (B) of Chinese Academy of Sciences (#XDB18000000). We are grateful to the two anonymous reviewers and the associate editor for their helpful comments to improve the manuscript and M. Walter for his handling as an editor. Z. Zhang acknowledges the supports from National Natural Science Foundation of China (41474156, 41020134003). All the simulations were carried out on the computational facilities in the Computer Simulation Lab of IGGCAS. The data for this paper can be found in the supporting information.

References

Biellmann, C., Gillet, P., Guyot, F., Peyronneau, J., & Reynard, B. (1993). Experimental-evidence for carbonate stability in the Earths lower mantle. *Earth and Planetary Science Letters*, *118*(1-4), 31–41. https://doi.org/10.1016/0012-821X(93)90157-5

Brenker, F. E., Vollmer, C., Vincze, L., Vekemans, B., Szymanski, A., Janssens, K., et al. (2007). Carbonates from the lower part of transition zone or even the lower mantle. *Earth and Planetary Science Letters*, *260*(1-2), 1–9. https://doi.org/10.1016/j.epsl.2007.02.038

Fei, Y. W., Ricolleau, A., Frank, M., Mibe, K., Shen, G. Y., & Prakapenka, V. (2007). Toward an internally consistent pressure scale. *Proceedings of the National Academy of Sciences of the United States of America*, *104*(22), 9182–9186. https://doi.org/10.1073/pnas.0609013104

Fiquet, G., & Reynard, B. (1999). High-pressure equation of state of magnesite: New data and a reappraisal. *American Mineralogist*, *84*(5-6), 856–860. https://doi.org/10.2138/am-1999-5-619

Gavryushkin, P. N., Martirosyan, N. S., Inerbaev, T. M., Popov, Z. I., Rashchenko, S. V., Likhacheva, A. Y., et al. (2017). Aragonite-II and $CaCO_3$-VII: New high-pressure, high-temperature polymorphs of $CaCO_3$. *Crystal Growth & Design*, *17*(12), 6291–6296. https://doi.org/10.1021/acs.cgd.7b00977

Hammouda, T., & Keshav, S. (2015). Melting in the mantle in the presence of carbon: Review of experiments and discussion on the origin of carbonatites. *Chemical Geology*, *418*, 171–188. https://doi.org/10.1016/j.chemgeo.2015.05.018

Hammouda, T., & Laporte, D. (2000). Ultrafast mantle impregnation by carbonatite melts. *Geology*, *28*(3), 283–285. https://doi.org/10.1130/0091-7613(2000)28<283:UMIBCM>2.0.CO;2

Holland, T. J., Hudson, N. F., Powell, R., & Harte, B. (2013). New thermodynamic models and calculated phase equilibria in NCFMAS for basic and ultrabasic compositions through the transition zone into the uppermost lower mantle. *Journal of Petrology*, *54*(9), 1901–1920. https://doi.org/10.1093/petrology/egt035

Huang, W.-L., & Wyllie, P. J. (1976). Melting relationships in the systems CaO-CO_2 and MgO-CO_2 to 33 kilobars. *Geochimica et Cosmochimica Acta*, *40*, 129–132.

Irving, A. J., & Wyllie, P. J. (1973). Melting relationships in CaO-CO_2 and MgO-CO_2 to 36 kilobars with comments on CO_2 in the mantle. *Earth and Planetary Science Letters*, *20*(2), 220–225. https://doi.org/10.1016/0012-821X(73)90161-1

Kakizawa, S., Inoue, T., Suenami, H., & Kikegawa, T. (2015). Decarbonation and melting in $MgCO_3$-SiO_2 system at high temperature and high pressure. *Journal of Mineralogical and Petrological Sciences*, *110*(4), 179–188. https://doi.org/10.2465/jmps.150124

Kaminsky, F. (2012). Mineralogy of the lower mantle: A review of 'super-deep' mineral inclusions in diamond. *Earth-Science Reviews*, *110*(1–4), 127–147. https://doi.org/10.1016/j.earscirev.2011.10.005

Keppler, H., Wiedenbeck, M., & Shcheka, S. S. (2003). Carbon solubility in olivine and the mode of carbon storage in the Earth's mantle. *Nature*, *424*(6947), 414–416. https://doi.org/10.1038/nature01828

Kresse, G., & Joubert, D. (1999). From ultrasoft pseudopotentials to the projector augmented-wave method. *Physical Review B*, *59*(3), 1758–1775. https://doi.org/10.1103/PhysRevB.59.1758

Li, X., Zhang, Z., Lin, J.-F., Ni, H., Prakapenka, V. B., & Mao, Z. (2018). New high pressure phase of $CaCO_3$ at the topmost lower mantle: Implication for the deep mantle carbon transportation. *Geophysical Research Letters*, *45*(3), 1355–1360. https://doi.org/10.1002/2017GL076536

Li, Y., Zou, Y. T., Chen, T., Wang, X. B., Qi, X. T., Chen, H. Y., et al. (2015). P-V-T equation of state and high-pressure behavior of $CaCO_3$ aragonite. *American Mineralogist*, *100*(10), 2323–2329. https://doi.org/10.2138/am-2015-5246

Li, Z. Y., Li, J., Lange, R., Liu, J. C., & Mintzer, B. (2017). Determination of calcium carbonate and sodium carbonate melting curves up to Earth's transition zone pressures with implications for the deep carbon cycle. *Earth and Planetary Science Letters*, *457*, 395–402. https://doi.org/10.1016/j.epsl.2016.10.027

Litasov, K. D. (2011). Physicochemical conditions for melting in the Earth's mantle containing a C-O-H fluid (from experimental data). *Russian Geology and Geophysics*, *52*(5), 475–492. https://doi.org/10.1016/j.rgg.2011.04.001

Litasov, K. D., Goncharov, A. F., & Hemley, R. J. (2011). Crossover from melting to dissociation of CO_2 under pressure: Implications for the lower mantle. *Earth and Planetary Science Letters*, *309*(3-4), 318–323. https://doi.org/10.1016/j.epsl.2011.07.006

Litasov, K. D., Shatskiy, A., Gavryushkin, P. N., Bekhtenova, A. E., Dorogokupets, P. I., Danilov, B. S., et al. (2017). P-V-T equation of state of $CaCO_3$ aragonite to 29 GPa and 1673 K: In situ X-ray diffraction study. *Physics of the Earth and Planetary Interiors*, *265*, 82–91. https://doi.org/10.1016/j.pepi.2017.02.006

Litasov, K. D., Shatskiy, A., Ohtani, E., & Yaxley, G. M. (2013). Solidus of alkaline carbonatite in the deep mantle. *Geology*, *41*(1), 79–82. https://doi.org/10.1130/G33488.1

Lobanov, S. S., Dong, X., Martirosyan, N. S., Samtsevich, A. I., Stevanovic, V., Gavryushkin, P. N., et al. (2017). Raman spectroscopy and X-ray diffraction of sp^3 $CaCO_3$ at lower mantle pressures. *Physical Review B*, *96*(10), 104101. https://doi.org/10.1103/PhysRevB.96.104101

Luth, R. W. (1999). Carbon and carbonates in the mantle. In Y. W. Fei, C. M. Bertka, & B. O. Mysen (Eds.), *Mantle petrology: Field observations and high pressure experimentation: A tribute to Francis R. (Joe) Boyd* (pp. 297–316). Geochemical Society.

Luth, R. W. (2014). Volatiles in Earth's mantle. In H. D. H. K. Turekian (Ed.), *Treatise on geochemistry* (2nd ed., pp. 355–391). Oxford: Elsevier. https://doi.org/10.1016/B978-0-08-095975-7.00207-2

Maeda, F., Ohtani, E., Kamada, S., Sakamaki, T., Hirao, N., & Ohishi, Y. (2017). Diamond formation in the deep lower mantle: A high-pressure reaction of $MgCO_3$ and SiO_2. *Scientific Reports*, *7*(1), 40602. https://doi.org/10.1038/srep40602

Martinez, I., Zhang, J. Z., & Reeder, R. J. (1996). In situ X-ray diffraction of aragonite and dolomite at high pressure and high temperature: Evidence for dolomite breakdown to aragonite and magnesite. *American Mineralogist*, *81*(5-6), 611–624. https://doi.org/10.2138/am-1996-5-608

Merlini, M., Hanfland, M., & Crichton, W. A. (2012). $CaCO_3$-III and $CaCO_3$-VI, high-pressure polymorphs of calcite: Possible host structures for carbon in the Earth's mantle. *Earth and Planetary Science Letters*, *333*, 265–271.

Monserrat, B., Drummond, N. D., & Needs, R. J. (2013). Anharmonic vibrational properties in periodic systems: Energy, electron-phonon coupling, and stress. *Physical Review B*, *87*(14), 144302. https://doi.org/10.1103/PhysRevB.87.144302

Oda, H., Anderson, O. L., Isaak, D. G., & Suzuki, I. (1992). Measurement of elastic properties of single-crystal CaO up to 1200-K. *Physics and Chemistry of Minerals*, *19*, 96–105.

Oganov, A. R., Glass, C. W., & Ono, S. (2006). High-pressure phases of $CaCO_3$: Crystal structure prediction and experiment. *Earth and Planetary Science Letters*, *241*(1-2), 95–103. https://doi.org/10.1016/j.epsl.2005.10.014

Oganov, A. R., & Ono, S. (2004). Theoretical and experimental evidence for a post-perovskite phase of $MgSiO_3$ in Earth's D″ layer. *Nature*, *430*(6998), 445–448. https://doi.org/10.1038/nature02701

Oganov, A. R., Ono, S., Ma, Y. M., Glass, C. W., & Garcia, A. (2008). Novel high-pressure structures of $MgCO_3$, $CaCO_3$ and CO_2 and their role in Earth's lower mantle. *Earth and Planetary Science Letters*, *273*(1-2), 38–47. https://doi.org/10.1016/j.epsl.2008.06.005

Ono, S., Kikegawa, T., & Ohishi, Y. (2007). High-pressure transition of $CaCO_3$. *American Mineralogist*, *92*(7), 1246–1249. https://doi.org/10.2138/am.2007.2649

Ono, S., Kikegawa, T., Ohishi, Y., & Tsuchiya, J. (2005). Post-aragonite phase transformation in $CaCO_3$ at 40 GPa. *American Mineralogist*, *90*(4), 667–671. https://doi.org/10.2138/am.2005.1610

Pickard, C. J., & Needs, R. J. (2015). Structures and stability of calcium and magnesium carbonates at mantle pressures. *Physical Review B*, *91*(10), 104101. https://doi.org/10.1103/PhysRevB.91.104101

Rohrbach, A., & Schmidt, M. W. (2011). Redox freezing and melting in the Earth's deep mantle resulting from carbon-iron redox coupling. *Nature*, *472*(7342), 209–212. https://doi.org/10.1038/nature09899

Seto, Y., Hamane, D., Nagai, T., & Fujino, K. (2008). Fate of carbonates within oceanic plates subducted to the lower mantle, and a possible mechanism of diamond formation. *Physics and Chemistry of Minerals*, *35*(4), 223–229. https://doi.org/10.1007/s00269-008-0215-9

Shatskiy, A. F., Litasov, K. D., & Palyanov, Y. N. (2015). Phase relations in carbonate systems at pressures and temperatures of lithospheric mantle: Review of experimental data. *Russian Geology and Geophysics*, *56*(1-2), 113–142. https://doi.org/10.1016/j.rgg.2015.01.007

Spivak, A. V., Litvin, Y. A., Ovsyannikov, S. V., Dubrovinskaia, N. A., & Dubrovinsky, L. S. (2012). Stability and breakdown of $(CaCO_3)$-C^{13} melt associated with formation of C^{13}-diamond in static high pressure experiments up to 43 GPa and 3900 K. *Journal of Solid State Chemistry*, *191*, 102–106. https://doi.org/10.1016/j.jssc.2012.02.041

Stixrude, L., & Lithgow-Bertelloni, C. (2011). Thermodynamics of mantle minerals - II. Phase equilibria. *Geophysical Journal International*, *184*(3), 1180–1213. https://doi.org/10.1111/j.1365-246X.2010.04890.x

Stixrude, L., Lithgow-Bertelloni, C., Kiefer, B., & Fumagalli, P. (2007). Phase stability and shear softening in $CaSiO_3$ perovskite at high pressure. *Physical Review B*, *75*(2), 024108. https://doi.org/10.1103/PhysRevB.75.024108

Suito, K., Namba, J., Horikawa, T., Taniguchi, Y., Sakurai, N., Kobayashi, M., et al. (2001). Phase relations of $CaCO_3$ at high pressure and high temperature. *American Mineralogist*, *86*(9), 997–1002. https://doi.org/10.2138/am-2001-8-906

Thomson, A. R., Walter, M. J., Kohn, S. C., & Brooker, R. A. (2016). Slab melting as a barrier to deep carbon subduction. *Nature*, *529*(7584), 76–79. https://doi.org/10.1038/nature16174

Thomson, A. R., Walter, M. J., Lord, O. T., & Kohn, S. C. (2014). Experimental determination of melting in the systems enstatite-magnesite and magnesite-calcite from 15 to 80 GPa. *American Mineralogist*, *99*(8-9), 1544–1554. https://doi.org/10.2138/am.2014.4735

Togo, A., & Tanaka, I. (2015). First principles phonon calculations in materials science. *Scripta Materialia*, *108*, 1–5. https://doi.org/10.1016/j.scriptamat.2015.07.021

Walter, M. J., Kohn, S. C., Araujo, D., Bulanova, G. P., Smith, C. B., Gaillou, E., et al. (2011). Deep mantle cycling of oceanic crust: Evidence from diamonds and their mineral inclusions. *Science*, *334*(6052), 54–57. https://doi.org/10.1126/science.1209300

Zedgenizov, D. A., Ragozin, A. L., Kalinina, V. V., & Kagi, H. (2016). The mineralogy of Ca-rich inclusions in sublithospheric diamonds. *Geochemistry International*, *54*(10), 890–900. https://doi.org/10.1134/S0016702916100116

Zen, E. A. (1966). Construction of pressure-temperature diagrams for multicomponent systems after the method of Shreinemakers: A geometric approach. *United States Geological Survey Bulletin*, *1225*, 1–56.

Zhang, D. B., Sun, T., & Wentzcovitch, R. (2014). Phonon quasiparticles and anharmonic free energy in complex systems. *Physical Review Letters*, *112*(5), 058501. https://doi.org/10.1103/PhysRevLett.112.058501

Zhang, Z. G., & Liu, Z. R. (2015). High pressure equation of state for molten $CaCO_3$ from first principles simulations. *Chinese Journal of Geochemistry*, *34*(1), 13–20. https://doi.org/10.1007/s11631-015-0036-8

Zhang, Z. G., Stixrude, L., & Brodholt, J. (2013). Elastic properties of $MgSiO_3$-perovskite under lower mantle conditions and the composition of the deep Earth. *Earth and Planetary Science Letters*, *379*, 1–12. https://doi.org/10.1016/j.epsl.2013.07.034